ACS OMEGA

http://pubs.acs.org/journal/acsodf

Article

Growth and High-Performance Photodetectors of $CsPbBr_3$ Single Crystals

Pengpeng Cheng, Zehan Liu, Ruyan Kang, Jian Zhou, Xiaoshan Wang, Jia Zhao, and Zhiyuan Zuo*

Cite This: *ACS Omega* 2023, 8, 26351−26358

Read Online

ACCESS | Metrics & More | Article Recommendations | Supporting Information

ABSTRACT: Organic−inorganic hybrid perovskites have demonstrated exceptional photovoltaic properties, making them highly promising for solar cells and photodetectors (PDs). However, the organic components of these materials are vulnerable to heat and strong light illumination, limiting their application prospects. All-inorganic cesium-based perovskite PDs, on the other hand, possess enhanced thermal tolerance and stability, making them ideal for perovskite applications. The utilization of a ternary mixture solvent and additives in combination with single crystal (SC) growth has enabled the production of highly crystalline SCs with a defect density of 3.79×10^9 cm^{-3}. The performance of the SC PDs had been evaluated using metal−semiconductor−metal devices, which demonstrated excellent results with a dark current as low as 0.198 μA at 10 V bias, on−off ratios exceeding 10^3, and a response time of shorter than 1 ms.

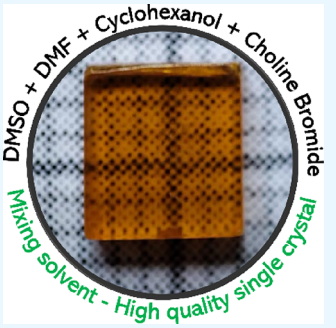

INTRODUCTION

Lead halide semiconductors with ABX_3 stoichiometry show great advantages and application potentials in light-emitting diodes, lasers, photodetectors (PDs), memristors, solar cells, and so on due to their excellent optoelectronic characteristics.[1−5] A lot of research has been reported in the field of photovoltaics on perovskite materials, and many methods have been proposed to improve the conversion efficiency of perovskite photovoltaic devices, such as improving crystallinity, optimizing interfaces, introducing additives, etc.[6] In perovskite devices, perovskite materials exist in various forms, such as polycrystalline films, single crystals (SCs), nanocrystals, quantum dots, etc., which also reflects the outstanding processability of perovskite.[7] This diversity of application forms is attributed to the defect tolerance of perovskite materials. The SCs possesses greater advantages in terms of carrier mobilities, environmental tolerance, etc. when compared to polycrystalline thin films.[8] Unfortunately, organic−inorganic hybrid perovskites become unstable under the condition of moisture, strong light, and high temperature, which limits the long-term stability of the device. The introduction of additives, enhancement of encapsulation, and substitution of organic components are among the strategies that have been suggested to augment the stability of devices.[9,10] The use of inorganic components to replace organic components is one of the most direct and promising methods, and cesium-based perovskites are a good choice. The tolerance factor of cesium-based all-inorganic perovskites is particularly appropriate, and these materials demonstrate long-term environmental stability without compromising many of their properties. Additionally, they are highly resistant to strong light illumination, high temperatures, and other such conditions.[11]

$CsPbBr_3$ exhibits remarkable optoelectronic properties such as a direct and tunable band gap, a long carrier diffusion length, a broad absorption spectra, and narrow emission spectra comparable to those of organic−inorganic hybrid perovskites.[12,13] In the past few years, $CsPbBr_3$ PDs have been widely studied. Although devices made from perovskite quantum dots and nanocrystals often have higher performance, the study of the optoelectronic properties of perovskite single crystals is more reflective of the material's nature and therefore optimization and research into single crystals is essential.[14,15] The $CsPbBr_3$ single crystal has excellent performance not only as a photodetector, but also as a high-energy particle and radiation detector. Due to the free of organic groups and the large atomic number of atoms, it is more stable under the action of high-energy particles and rays than organic inorganic perovskites.[16−18] Most of the reports utilized polycrystalline thin films, nanocrystals, and quantum dots.[19,20] The growth of large SCs has always been a critical technology. For instance, large SC ingots are commonly utilized in the most state-of-the-art semiconductor industry to process devices. Therefore, there is a high demand for $CsPbBr_3$ SC suitable for PDs to explore the inherent properties of $CsPbBr_3$ and thus bridge the differences with its polycrystalline counterparts. For $CsPbBr_3$ SCs, two main growth methods are the Bridgman method and the solution growth method, respectively. Song et al. obtained

Received: April 27, 2023
Accepted: July 5, 2023
Published: July 13, 2023

https://doi.org/10.1021/acsomega.3c02888
ACS Omega 2023, 8, 26351−26358

large $CsPbBr_3$ ingots using the Bridgman method and realized a visible-infrared dual-mode PD.[21] Ding et al. fabricated $CsPbBr_3$ SCs using the solution method and investigated their performance as PDs.[22] Li et al. demonstrated that $CsPbBr_3$ SCs exhibit remarkable performance in X-ray and gamma-ray detection, fabricated a high-performance X-ray detector with $CsPbBr_3$ SCs, and investigated the effect of rubidium doping on the detection performance.[23] Pan et al. reported the performance of gamma-ray detection using $CsPbBr_3$ devices.[24] We found that $CsPbBr_3$ SCs grown by either high energy-consuming melt method or solution method were not transparent and the interior of the SC always showed a turbid state, which may be related to the high quantity of defects.

In this work, we demonstrated an improved additive-assisted solution crystallization method for the growth of high-quality $CsPbBr_3$ SCs. Additives facilitate the growth of $CsPbBr_3$ SCs into cuboid shapes and prevent the growth of rod-like SCs. The improved solvent system smoothed the precursor solubility with temperature and reduced the oversaturation, which was beneficial to reduce the number of nucleation and inhibiting the formation of polycrystals. We also investigated the rapid and delicate detection of $CsPbBr_3$ to visible light with optimized SC response times of less than 1 ms and on−off ratios of more than 10^3, demonstrating that the optimized solution-cultivated SC has a lower trap density and increased crystallinity.

RESULTS AND DISCUSSION

We have compiled the pros and cons of multiple solution growth techniques and put forward a unique additive-assisted solution growth technique: CsBr:$PbBr_2$ of 1:2 in the precursor solution to avoid cesium-rich or lead-rich products; adding the additive choline bromide to inhibit growth in the [002] direction; using a ternary solvent mixture of DMSO:dimethylformamide (DMF):cyclohexanol to optimize the solubility trend with temperature; lowering the crystallization temperature to 80 °C in order to avoid the phase transition during the cooling process; and finally, the growth vessel at the top with air holes to maintain sustainable crystallization by controlling the evaporation of the solvent. Figure S1a shows a single crystal grown in DMSO solvent using the inverse temperature growth method, showing a long rod shape. Figure S1b shows a single crystal grown in DMSO solvent assisted by the addition of choline bromide, showing a cubic shape. Although crystals showing a better cuboid shape were grown, the interior of the crystals showed a turbid state, which suggests the presence of several crystal defects inside the crystals. We suggest that the defects inside the crystal are caused by the rapid change in solubility, which does not give enough time for the crystal defects to be eliminated, and therefore the defects remain inside the crystal showing a turbid state. To obtain a smooth solubility variation, one is to precisely control the temperature and the rate of temperature change, which will inevitably put higher demands on the growth equipment and thus increase the growth cost; the other is using a new solution system to regulate the trend of precursor solubility change with temperature to make it smooth. Figure S1c shows $CsPbBr_3$ single crystals grown in a DMSO:DMF:cyclohexanol ternary solvent mixture. $CsPbBr_3$ single crystals show a translucent appearance, which benefits from a flattening of the solubility trend with temperature. $CsPbBr_3$ single crystals have a phase transition around 85°, so using a growth temperature below 85° helps to reduce the effect of the phase transition on crystal quality. Impressive among these is the contribution of the additive choline bromide. The choline cation will adsorb to the surface of the halogen atoms exposed by the single crystal by electrostatic interaction, which will result in the adsorption of Cs^+ and Pb^{2+} being inhibited. It is worth noting that the (001) and (110) surfaces have the same density of halogen surfaces and therefore the choline cation interacting with the (001) surface will also interact with the (110) surface. The (001) surface was found to be more inhibited than the (110) surface in the experiment, resulting in a reduced difference in growth rate between the two directions.[25]

Unlike the high temperatures and inert atmospheres required for the synthesis of perovskite quantum dots, the growth of perovskite single crystals requires lower temperatures and does not require inert atmosphere protection.[26] The growth of perovskite microcrystals is usually obtained using solvent volatilization, which produces single crystals of micron size. Using this method, it is difficult to grow large single crystals of high quality and tends to lead to polycrystallization.[27−29] The development of techniques for the growth of large single crystals of perovskite is warranted. The experimental growth of large perovskite single crystals using the inverse temperature method is very simple. The precursor solution is put in a glass vial and the temperature of the precursor solution is raised uniformly by heating in an oil bath, and over a period of time, the grown crystals can be found at the bottom of the vessel. When crystals are grown at the edge of the bottle, space constraints will lead to a change in the shape of the grown single crystal. The $CsPbBr_3$ SC grown by the optimized SC growth method is shown in Figure S1d,e, which shows excellent transparency. The growth of the crystals at different time intervals is shown in Figure S2. The size of the crystals grown by the optimized method (treatment crystal) has increased to 8 mm. The crystals grown by the choline bromide-only method were used as the control crystals, and we did a series of comparisons.

PL spectra are presented in Figure 1a, the full width at half-maximum (FWHM) of the treatment crystals is 14.6 nm,

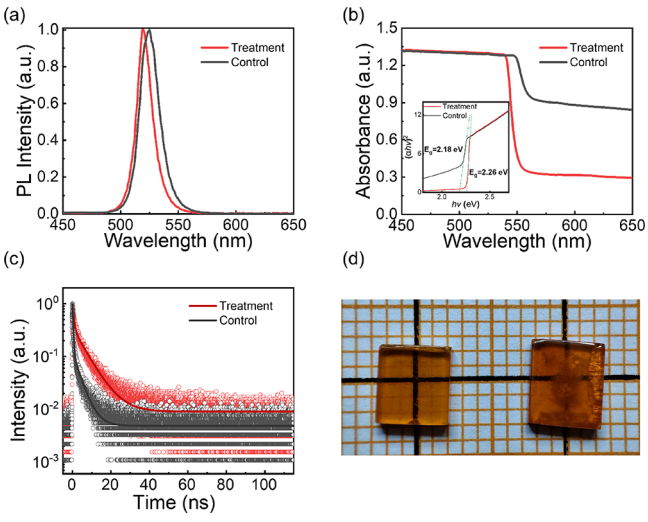

Figure 1. (a) Control crystal and treatment crystal photoluminescence (PL) spectra. (b) UV−Visible absorption spectra, the inset is band gap calculation with a Tauc plot. (c) Time-resolved PL decay spectra of control crystal and treatment crystal. (d) Optical photos of the control crystal (right) and the treatment crystal (left).

https://doi.org/10.1021/acsomega.3c02888
ACS Omega 2023, 8, 26351−26358

which is 4.1 nm narrower than the control crystals. Also, the peak of the treatment crystals is located at 519.9 nm with a blue shift of 5.3 nm compared to the control crystals, which usually means fewer shallow defects and higher quality of the same material.[30,31] We use microzonal spectroscopy equipment to collect photoluminescence spectra of the sample from a microscope directly above to receive the PL signal. The shape dependence of the spectra mentioned in previous reports arises from perovskite microcrystals, which have a huge surface-to-volume (s-t-v), and the dependence decreases as s-t-v decreases.[3] The s-t-v of our fabricated single crystal is estimated to be 0.002 μm^{-1}, and the shape dependence of such a small s-t-v becomes very small. Also, the excitation light at 375 nm has a very shallow depth of action. Therefore, the spectral shape of our sample does not have much internal filtering effect. As evidenced by Figure 1b, the UV−visible absorption spectra of the two crystals were collected, revealing that the treatment crystal exhibited a much lower absorption when the wavelength exceeded the band-edge, suggesting reduced defect scattering and absorption levels. The absorption spectra were fitted by a direct bandgap Tauc plot (Figure 1b) with a bandgap of about 2.26 eV for the treatment crystals, which is similar to the previously reported bandgap of $CsPbBr_3$ SC grown by the Bridgman method.[32] The band gap of the control crystal is about 2.18 eV, which is similar to the previously reported $CsPbBr_3$ SC grown by the solution method, indicating a high level of near-edge defects in the control crystal.[22] Time-resolved PL is a non-contact probe technique that detects the effects of impurities and defects in semiconductor samples.[33] The time-resolved PL decay of the two crystals is shown in Figure 1c, which fits the bi-exponential decay. τ_1 is called faster decay time corresponding to trap-assisted recombination, and τ_2 is called slower decay time corresponding to free carrier recombination. τ_1 and τ_2 of the control crystal are 0.32 and 2.97 ns, respectively, and those of the treatment crystal are 0.70 and 6.51 ns, respectively. Both τ_1 and τ_2 of the treatment crystal are longer than those of the control crystal, which indicates the reduction of traps in the treatment crystal.[34]

XRD patterns of Figure 2a show that both crystals are orthorhombic structures, which match the PDF card and the calculated results.[35] In addition, we also collected XRD patterns of single crystals (Figure 2b). The FWHM of the (110) plane of the treatment crystal is 0.082° (Figure 2b), narrower than that of the control crystal by 0.011°. Also, it is shifted to a higher angle by 0.022°, which usually means a better crystallinity.[36] For an accurate analysis of the FWHM of the XRD, we fitted the diffraction peaks generated on the surface of (110). Using the Gaussian fitting model, the corresponding equations and parameters are given in eq 1 and Table S6.

$$y = y_0 + \left(\frac{A}{w\sqrt{\frac{\pi}{2}}} \times e^{-2\left(\frac{x-x_c}{w}\right)^2} \right) \quad (1)$$

The V_{TFL} for the control and treatment crystals was determined by the space-charge-limited-current technique to be 10.66 and 7.01, respectively, as shown in Figure 2c. By fitting the $I-V$ curve, we can obtain the trap density and carrier mobility of the SCs.

The trap density (n_t) can be estimated using eq 2

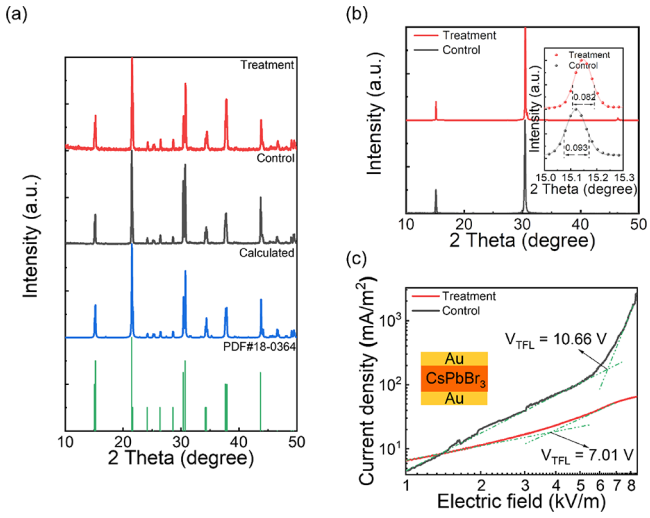

Figure 2. (a) Powder X-ray diffraction (XRD) patterns of two SCs with PDF card and simulation results of $CsPbBr_3$. (b) XRD of the surface of two single crystals (110), the inset solid line is the result of a Gauss fitting and corresponds to a detailed plot of the diffraction peaks on the crystalline surface (110). (c) $I-V$ characteristics of devices of the two crystals. The inset shows the device structure.

$$n_t = \frac{2\varepsilon\varepsilon_0 V_{TFL}}{ed^2} \quad (2)$$

where the relative permittivity ε of $CsPbBr_3$ is 16.4, ε_0 is the vacuum dielectric constant, V_{TFL} is the trap-filled limit voltage, and d is the perovskite depth.[37] Defects are inherent in perovskites and act as compound centers affecting the quantum yield of perovskite materials, leading to reduced efficiency when perovskites are used as solar cells or light emitting diodes, and some macroscopic defects can also lead to fragmentation of single crystal materials. Therefore, the preparation of single crystals with low defect density is necessary.[38] The trap densities of the control and treatment crystals are 7.10×10^9 and 3.79×10^9 cm^{-3}, respectively. The treatment crystal has lower trap density, which also verifies the conclusion of the spectral characterization. We compared the previous reported trap densities of $CsPbBr_3$, and we fabricated single crystals with lower defect densities, as shown in Table S1.

Scanning electron microscopy (SEM) images of the two SCs are shown in Figure S3a,b, and their elemental stoichiometry was characterized by energy-dispersive X-ray spectroscopy (EDS) as shown in Figure S3c,d. The single crystal surface is proven to be smooth and flat, and the elemental ratio is close to 1:1:3. TGA, FTIR, and Raman measurements of the treatment samples are shown in Figure S5. As shown in Figure S5a, in the Raman spectrum, we can only observe the $PbBr_6$ cage related bending vibrations at 65 cm^{-1} and cationic libration at 141 cm^{-1}.[39,40] The carbon−carbon bond stretching at 1049 cm^{-1} and hydroxyl group stretching at 2950 cm^{-1}, corresponding to cyclohexanol, do not appear in the Raman spectrum.[41] Figure S5b shows the FTIR spectrum of the powder. The perovskite single crystals were crushed and mixed into KBr-pressed samples, and it was difficult to avoid the interference of moisture in the test because the perovskite powder has a strong hygroscopic nature. In Gordon et al., it was reported that KBr showed significant interference peaks in FTIR after a short period of moisture absorption, corresponding to 1680, 2119, 2850, 2928, and 3450 cm^{-1} in Figure S5b.[42]

https://doi.org/10.1021/acsomega.3c02888
ACS Omega 2023, 8, 26351−26358

Zhang et al. used $CsPbBr_3$ single crystals for direct FTIR measurements, and the same water-induced interference peaks appeared.[43] Also, the spectrum does not show the characteristic peak of 1366 cm^{-1} corresponding to cyclohexanol.[44] As shown in Figure S5c, the boiling point of cyclohexanol is 159° and we did not find any loss of weight near 159° in our TGA tests. The samples were heated to 500° in steps of 10° per minute, under nitrogen blowing conditions. Due to the limitations of the equipment for chloride measurement, heating was only to 500°. All of these results above indicate that there is no alcohol inclusion in the single crystals.

Our $I-V$ characteristic curves are prepared by magnetron sputtering of an inserted finger gold electrode onto the surface of a perovskite single crystal. Two probe electrodes are connected to the left and right side of the inserted finger electrode, bias voltage is applied, and the current signal of the device is collected using the Keithley 4200A. The single crystal detector uses a planar structure where gold inserted finger electrodes are prepared onto the polished single crystal surface. Thin film detectors are classified into vertical structures, which are sandwich structures with an active layer between the upper and lower electrodes, and lateral structures, where perovskite is prepared onto side-by-side electrodes. Figure 3 shows the $I-V$

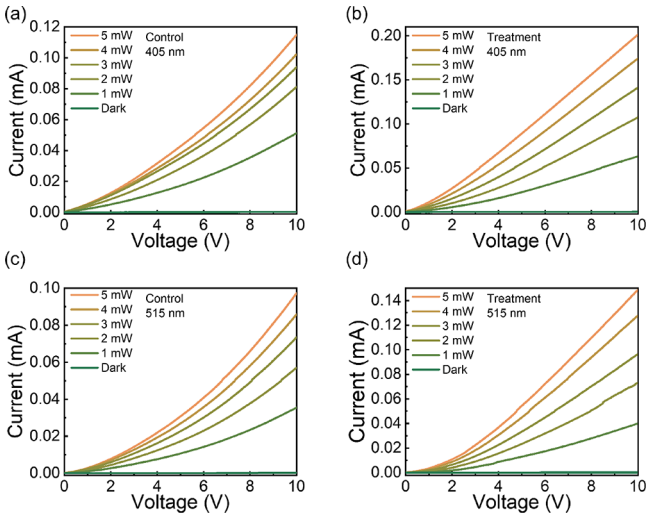

Figure 3. $I-V$ curves of the crystals at different wavelengths and powers of excitation light and $I-V$ curves in dark conditions. (a) Control crystal and (b) treatment crystal under 405 nm excitation light. (c) Control crystal and (d) treatment crystal under 515 nm excitation light.

curves of two $CsPbBr_3$ SCs measured under laser irradiation of 405 and 515 nm wavelengths, respectively. With the optical power of laser increasing from 1 to 5 mW (Figure S4). At a bias voltage of 10 V, the dark current of control crystal is 0.23 μA and the treatment crystal is as low as 0.20 μA. The on−off ratios of the control crystal and the treatment crystal reach 508 and 1017, respectively, at a bias voltage of 10 V @5 mW 405 nm; when 10 V @5 mW 515 nm, conditions are 430 and 752, respectively.

Figure 4 shows the responsivity and EQE of both crystals at different wavelengths, respectively. The responsivity and EQE are calculated by eqs 3 and 4:

$$R = \frac{I_{irra} - I_{dark}}{P_{irra}} \tag{3}$$

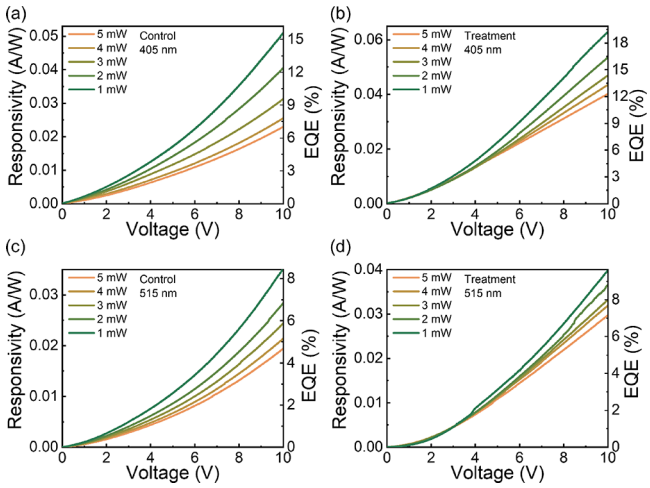

Figure 4. Responsivities and external quantum efficiency (EQE) of the crystals under different wavelengths and powers of excitation light. (a) Control crystal and (b) treatment crystal under 405 nm excitation light. (c) Control crystal and (d) treatment crystal under 515 nm excitation light.

and

$$EQE = \frac{R \cdot hc}{e\lambda} \tag{4}$$

where I_{irra} and I_{dark} are the currents measured under excitation light irradiation and dark conditions, respectively. P_{irra} is the power irradiated by the excitation light, and λ is the wavelength of the irradiated light. Both responsivity and EQE can reveal the conversion ratio of irradiated power to photocurrent, which depend on the incident optical power density and applied voltage. Because two incident wavelengths of 405 and 515 nm were applied to both crystals during the measurements in this study, the responsivity and EQE were expressed in four groups of curves. While the wavelength is 405 nm, the irradiation power is 1 mW, and the applied voltage is 10 V, the maximum responsivity and EQE of the control crystal are 0.051 A/W and 15.6%, respectively, and the maximum responsivity and EQE of the treatment crystal under the same conditions are 0.063 A/W and 19.3%, respectively. For 515 nm, the irradiation power remains at 1 mW, the bias voltage remains at 10 V, the maximum responsivity and EQE of the control crystal are 0.035 A/W and 8.5%, respectively, and the maximum responsivity and EQE of the treatment crystal are 0.040 A/W and 9.6%, respectively.

The detectivity of a perovskite SC PD can be expressed according to eq 5:

$$D = \frac{R}{(2q \cdot I_{dark})^{1/2}} \tag{5}$$

where q, R, and I_{dark} are the elementary charge, responsivity, and dark current, respectively. As shown in Figure 5a,b, the maximum detectivities of the control crystal and the treatment crystal are 1.89×10^{11} and 2.06×10^{11} Jones, respectively, under a light power of 1 mW and wavelength of 405 nm. The maximum detectivities of the control crystal and the treatment crystal at the same power of 1 mW and 515 nm are 1.15×10^{11} and 1.58×10^{11} Jones, respectively, Figure 5c,d. Our detectors have a higher detectivity for light with shorter wavelengths, a difference that is due to the band gap and surface compounding of the active layer. Also, the detector has a

https://doi.org/10.1021/acsomega.3c02888
ACS Omega 2023, 8, 26351−26358

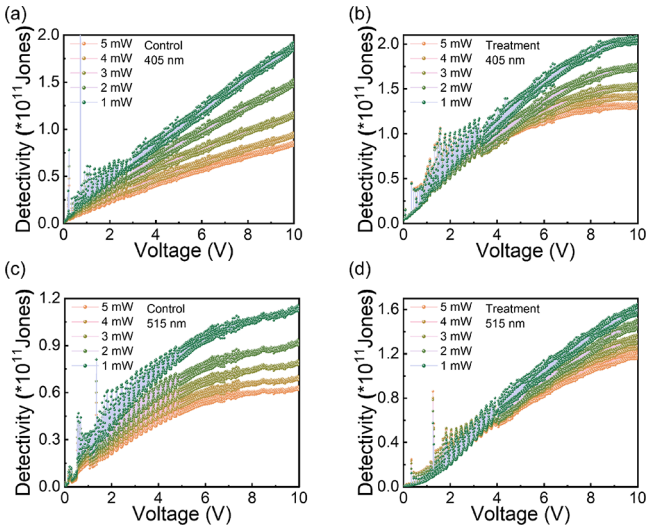

Figure 5. Detectivity of the devices under the action of excitation light of different wavelengths and powers. (a) Control crystal and (b) treatment crystal under 405 nm excitation light. (c) Control crystal and (d) treatment crystal under 515 nm excitation light.

better detectivity for low power light, as reported in its research in the field of weak light imaging applications. Single crystal photodetectors have a much different order of electrode fabrication than the common perovskite thin film detectors. Thin film detectors are usually fabricated from perovskite onto the surface of prepared electrodes with structures to achieve the detection signal, such as vertical and lateral electrodes.[45−47] In contrast, single crystal detectors are prepared on the surface of grown single crystals, which are usually centimeter-thick and use flat electrodes in order to achieve good signal derivation, which have a smaller contact area with the active layer than vertical and lateral electrodes.

The response time is also an important parameter of the PD, and we collected the switching characteristics of the device at different wavelengths and different bias voltages with an incident power of 5 mW (Figure 6). The rise time and decay time of the device with different light powers and different bias voltages are summarized in Tables S2−S5. There is no significant relationship between the switching characteristics and the bias voltage. It has been observed that the crystal exhibits a rapid response to the light signal; specifically, when the bias voltage reaches 10 V, the rise time and decay time of the response to 405 nm excitation light are 0.33 ms.

CONCLUSIONS

High-quality $CsPbBr_3$ SCs were successfully obtained by the solution method with optimized growth conditions. The crystal exhibits a trap density as low as 3.79×10^9 cm^{-3}. The PD device fabricated using the high-quality $CsPbBr_3$ SCs exhibits remarkable performances, with a dark current of 0.198 μA at 10 V bias, on−off ratio of greater than 10^3, and response time of less than 1 ms. This research provides a facile and effective strategy for high-performance $CsPbBr_3$ PDs and other optoelectronic applications of $CsPbBr_3$.

EXPERIMENTAL SECTION

Materials. CsBr (99.0%), $PbBr_2$ (99.9%), and cyclohexanol (98.5%) are from Aladdin. DMSO (analytically pure 99.5%), and DMF (analytically pure 99.5%) were purchased from

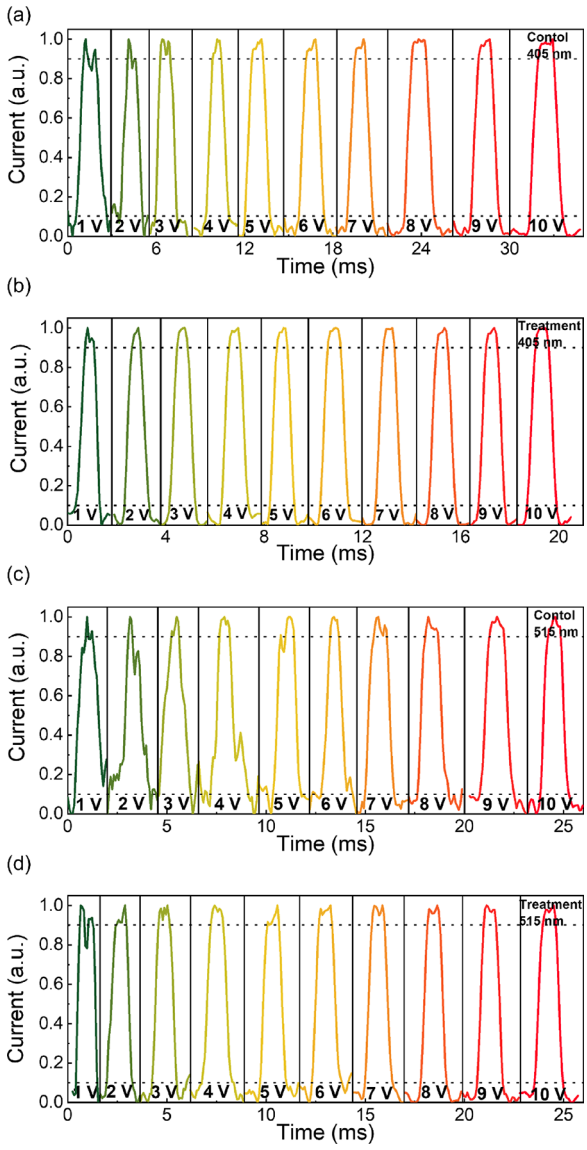

Figure 6. Transient photocurrent response of the device under the action of excitation light at different voltages and different wavelengths. (a) Control crystal and (b) treatment crystal under 405 nm excitation light. (c) Control crystal and (d) treatment crystal under 515 nm excitation light.

Hushi. Choline bromide was purchased from Macklin Corporation. All chemical raw materials and solvents were purchased and used directly without further purification.

Single Crystal Growth. Growth of the control SC: in 5.3 mL of DMSO solution, CsBr (2.4 mmol) and $PbBr_2$ (4.8 mmol) were added in a molar ratio of 1:2, and finally 0.25 mmol CB was added. The solution was stirred overnight on a hot plate at 60 °C and then filtered through a 0.22 μm PTFE filter, and the clear solution was transferred to a vial. The vial was set at 85 °C, and a perforated cap was used to promote solvent evaporation, which was used to provide a sustained growth driving force that would take out the crystals in about 100 h.

Growth of the treatment SC: DMSO, DMF, and cyclohexanol were mixed in the ratio of 20:7:3 to obtain the solvent mixture. The mixed solvent was used to dissolve 0.7 M CsBr, 1.4 M $PbBr_2$, and 0.02 M choline bromide. The solution was heated and stirred on a hot plate at 60 °C. The solution was

https://doi.org/10.1021/acsomega.3c02888
ACS Omega 2023, 8, 26351−26358

filtered through a 0.22 μm filter, and the solution was transferred to a vial after filtration. The vials were put in silicone oil at 80 °C, and the caps were staked out with an appropriate number of air holes. The sustained driving force for growth was supersaturation obtained by slow evaporation of the solvent. High-quality crystals of centimeter size are taken out of the solution around 100 h.

Device Fabrication. Well-polished SC surfaces before fabricating PDs. Gold-interdigitated electrodes were prepared using radio frequency (RF) sputtering with metal masks on the SC surface.

Characterizations and Measurements. The surface morphology and elemental ratios of the SCs were obtained using field emission SEM (Hitachi S-4800). The 375 nm laser (Pico Quant, Taiko PDL M1) was used as the excitation source, and the PL spectra were collected using NOVA 2000 (Ideaoptics). UV−Vis absorption spectra were collected using V-5100. Powder XRD patterns of SCs were collected by Smart APEX II (Bruker AXS). The 2θ range was set to 10−50° steps of 0.02°. The I−V and transient currents of the PDs are collected by a semiconductor parametric analysis system (Keithley 4200A-SCS, USA) and a manual high-precision probe station (KARL SUSS, PM5, Germany). A semiconductor laser was used as the excitation light source whose spectral characteristics are shown in Figure S5, and the intensity of the light was calibrated by an optical power meter (SANWA, LP1, Japan).

■ ASSOCIATED CONTENT

Supporting Information

The Supporting Information is available free of charge at https://pubs.acs.org/doi/10.1021/acsomega.3c02888.

> Single crystals grown under different conditions; SEM and EDS; photographs of devices; Raman, IR and thermogravimetry of samples; comparison of defect densities; response times; XRD fitted parameters (PDF)

■ AUTHOR INFORMATION

Corresponding Author

Zhiyuan Zuo − *Center for Optics Research and Engineering and Key Laboratory of Laser & Infrared System (Shandong University), Ministry of Education, Shandong University, Qingdao 266237, P. R. China; Institute of Novel Semiconductors, Shandong University, Jinan 250100, P. R. China;* orcid.org/0000-0002-3261-9217; Email: zuozhiyuan@sdu.edu.cn

Authors

Pengpeng Cheng − *Center for Optics Research and Engineering, Shandong University, Qingdao 266237, P. R. China; Institute of Novel Semiconductors, Shandong University, Jinan 250100, P. R. China*

Zehan Liu − *Center for Optics Research and Engineering, Shandong University, Qingdao 266237, P. R. China; Institute of Novel Semiconductors, Shandong University, Jinan 250100, P. R. China*

Ruyan Kang − *Key Laboratory of Laser & Infrared System (Shandong University), Ministry of Education, Shandong University, Qingdao 266237, P. R. China*

Jian Zhou − *Center for Optics Research and Engineering, Shandong University, Qingdao 266237, P. R. China; Institute of Novel Semiconductors, Shandong University, Jinan 250100, P. R. China*

Xiaoshan Wang − *Center for Optics Research and Engineering, Shandong University, Qingdao 266237, P. R. China; Institute of Novel Semiconductors, Shandong University, Jinan 250100, P. R. China*

Jia Zhao − *School of Information Science and Engineering, Shandong University, Qingdao 266237, P. R. China; Institute of Novel Semiconductors, Shandong University, Jinan 250100, P. R. China*

Complete contact information is available at: https://pubs.acs.org/10.1021/acsomega.3c02888

Notes

The authors declare no competing financial interest.

■ ACKNOWLEDGMENTS

This work was financially supported by the National Key R&D Program of China (Grant 2022YFB2802403, 2018YFA0209001), the National Natural Science Foundation of China (Grant 51702186), the Young Scholars Program of Shandong University, and the Natural Science Foundation of Shandong Province of China (Grant 2022HWYQ-019).

■ REFERENCES

(1) Zhao, F.; Ren, A.; Li, P.; Li, Y.; Wu, J.; Wang, Z. Toward Continuous-Wave Pumped Metal Halide Perovskite Lasers: Strategies and Challenges. *ACS Nano* **2022**, *16*, 7116−7143.

(2) Lin, K.; Xing, J.; Quan, L. N.; Arquer, F. P.; Gong, X.; Lu, J.; Xie, L.; Zhao, W.; Zhang, D.; Yan, C.; Li, W.; Liu, X.; Lu, Y.; Kirman, J.; Sargent, E. h.; Xiong, Q.; Wei, Z. Perovskite light-emitting diodes with external quantum efficiency exceeding 20 per cent. *Nature* **2018**, *562*, 245−245.

(3) Wang, H. P.; Li, S.; Liu, X.; Shi, Z.; Fang, X.; He, J. H. Low-Dimensional Metal Halide Perovskite Photodetectors. *Adv. Mater.* **2021**, *33*, 2003309.

(4) Liu, Z.; Cheng, P.; Li, Y.; Kang, R.; Zhang, Z.; Zuo, Z.; Zhao, J. High Temperature CsPbBrxI3−x Memristors Based on Hybrid Electrical and Optical Resistive Switching Effects. *ACS Appl. Mater. Interfaces* **2021**, *13*, 58885−58897.

(5) Dey, A.; Ye, J.; De, A.; Debroye, E.; Ha, S. K.; Bladt, E.; Kshirsagar, A. S.; Wang, Z.; Yin, J.; Wang, Y.; Quan, L. N.; Yan, F.; Gao, M.; Li, X.; Shamsi, J.; Debnath, T.; Cao, M.; Scheel, M. A.; Kumar, S.; Steele, J. A.; Gerhard, M.; Chouhan, L.; Xu, K.; Wu, X.; Li, Y.; Zhang, Y.; Dutta, A.; Han, C.; Vincon, I.; Rogach, A. L.; Nag, A.; Samanta, A.; Korgel, B. A.; Shih, C.; Gamelin, D. R.; Son, D. H.; Zeng, H.; Zhong, H.; Sun, H.; Demir, H. V.; Scheblykin, I. G.; Mora-Sero, I.; Stolarczyk, J. K.; Zhang, J. Z.; Feldmann, J.; Hofkens, J.; Luther, J. M.; Perez-Prieto, J.; Li, L.; Manna, L.; Bodnarchuk, M.; Kovalenko, M.; Roeffaers, M. B. J.; Pradhan, N.; Mohammed, O. F.; Bakr, O. M.; Yang, P.; Muller-Buschbaum, P.; Kamat, P.; Bao, Q.; Zhang, Q.; Krahne, R.; Galian, R. E.; Stranks, S. D.; Bals, S.; Biju, V.; Tisdale, W. A.; Yan, Y.; Hoye, R. L. Z.; Polavarapu, L. State of the art and Prospects for halide perovskite nanocrystals. *ACS Nano* **2021**, *15*, 10775−10981.

(6) Zhang, H.; Ji, X.; Yao, H.; Fan, Q.; Yu, B.; Li, J. Review on efficiency improvement effort of perovskite solar cell. *Sol. Energy* **2022**, *233*, 421−434.

(7) Kim, M. K.; Munkhsaikhan, Z.; Han, S. G.; Park, S. M.; Jin, H.; Cha, J.; Yang, S. J.; Seo, J.; Lee, H. S.; Choi, C. J.; Kim, M. Structural engineering of single-crystal-like perovskite nanocrystals for ultra-sensitive photodetector applications. *J. Mater. Chem. C* **2022**, *10*, 11401−11411.

(8) Ren, X.; Yang, Z.; Yang, D.; Zhang, X.; Cui, D.; Liu, Y.; Wei, Q.; Fan, H.; Liu, S. Modulating crystal grain size and optoelectronic

properties of perovskite films for solar cells by reaction temperature. *Nanoscale* **2015**, *8*, 3816−3822.
(9) Ma, S.; Yuan, G.; Zhang, Y.; Yang, N.; Li, Y.; Chen, Q. Development of encapsulation strategies towards the commercialization of perovskite solar cells. *Energy Environ. Sci.* **2022**, *15*, 13−55.
(10) Zhang, F.; Zhu, K. Additive Engineering for Efficient and Stable Perovskite Solar Cells. *Adv. Energy Mater.* **2020**, *10*, 1902579.
(11) Li, B.; Zhang, Y.; Xu, Y.; Xia, Z. Design optimization of $CsPbBr_3$ nanocrystals into zeolite Beta composites as ultra-stable green emitters for backlight display applications. *J. Mater. Chem. C* **2021**, *9*, 12118−12123.
(12) Tong, G.; Chen, T.; Li, H.; Qiu, L.; Liu, Z.; Dong, Y.; Song, W.; Ono, L. K.; Jiang, Y.; Qi, Y. Phase transition induced recrystallization and low surface potential barrier leading to 10.91%-efficient $CsPbBr_3$ perovskite solar cells. *Nano Energy* **2019**, *65*, No. 104015.
(13) Du, X.; Wu, G.; Cheng, J.; Dang, H.; Ma, K.; Zhang, Y. W.; Tan, P. F.; Chen, S. High-quality $CsPbBr_3$ perovskite nanocrystals for quantum dot light-emitting diodes. *RSC Adv.* **2017**, *7*, 10391−10396.
(14) Liu, D.; Hu, Z.; Hu, W.; Wang, P.; Yu, K.; Wen, M.; Zu, Z.; Liu, J.; Wang, M.; Chen, W.; Zhou, M.; Tang, X.; Zang, Z. Two-step method for preparing all-inorganic $CsPbBr_3$ perovskite film and its photoelectric detection application. *Mater. Lett.* **2017**, *186*, 243−246.
(15) Park, B.; Kang, S.; Lee, G.; Kwak, C. H.; Rethinasabapathy, M.; Huh, Y. S. Fabrication of $CsPbBr_3$ Perovskite Quantum Dots/Cellulose-Based Colorimetric Sensor: Dual-Responsive On-Site Detection of Chloride and Iodide Ions. *Ind. Eng. Chem. Res.* **2020**, *59*, 793−801.
(16) He, Y.; Petryk, M.; Liu, Z.; Chica, D. G.; Hadar, I.; Leak, C.; Ke, W.; Spanopoulos, I.; Lin, W.; Chung, D. Y.; Wessels, B. W.; He, Z.; Kanatzidis, M. G. CsPbBr3 perovskite detectors with 1.4% energy resolution for high-energy γ-rays. *Nat. Photonics* **2021**, *15*, 36−42.
(17) He, Y.; Liu, Z.; McCall, K. M.; Lin, W.; Chung, D. Y.; Wessels, B. W.; Kanatzidis, M. G. Perovskite $CsPbBr_3$ single crystal detector for alpha-particle spectroscopy. *Nucl. Instrum. Methods Phys. Res. Sect. A-Accel. Spectrom. Dect. Assoc. Equip.* **2019**, *922*, 217−221.
(18) He, Y.; Hadar, I.; De Siena, M. C.; Klepov, V. V.; Pan, L.; Chung, D. Y.; Kanatzidis, M. G. Sensitivity and Detection Limit of Spectroscopic-Grade Perovskite $CsPbBr_3$ Crystal for Hard X-Ray Detection. *Adv. Funct. Mater.* **2022**, *32*, 2112925.
(19) Zhu, W.; Deng, M.; Chen, D.; Chen, D. Z.; XI, H.; Chang, J.; Zhang, J.; Zhang, C.; Hao, Y. Sacrificial additive-assisted film growth endows self-powered $CsPbBr_3$ photodetectors with ultra-low dark current and high sensitivity. *J. Mater. Chem. C* **2020**, *8*, 209−218.
(20) Yan, S.; Tang, S.; Luo, M.; Xue, L.; Liu, S.; Elemike, E. E.; Bae, B. S.; Akram, J.; Chen, J.; Zhao, Z.; Zhu, Z.; Zhang, X.; Lei, W.; Li, Q. Surface passivation by congeneric quantum dots for high-performance and stable $CsPbBr_3$-based photodetectors. *J. Mater. Chem. C* **2021**, *9*, 10089−10100.
(21) Song, J.; Cui, Q.; Li, J.; Xu, J.; Wang, Y.; Xu, L.; Xue, J.; Dong, Y.; Tian, T.; Sun, H.; Zeng, H. Ultralarge All-Inorganic Perovskite Bulk Single Crystal for High-Performance Visible−Infrared Dual-Modal Photodetectors. *Adv. Opt. Mater.* **2017**, *5*, 1700157.
(22) Ding, J.; Du, S.; Zuo, Z.; Zhao, Y.; Cui, H.; Zhan, X. High Detectivity and Rapid Response in Perovskite $CsPbBr_3$ Single-Crystal Photodetector. *J. Phys. Chem. C* **2017**, *121*, 4917−4923.
(23) Li, J.; Du, X.; Niu, G.; Xie, H.; Chen, Y.; Yuan, Y.; Gao, Y.; Xiao, H.; Tang, J.; Pan, A.; Yang, B. Rubidium Doping to Enhance Carrier Transport in $CsPbBr_3$ Single Crystals for High-Performance X-Ray Detection. *ACS Appl. Mater. Interfaces* **2020**, *12*, 989−996.
(24) Pan, L.; Feng, Y.; Kandlakunta, P.; Huang, J.; Cao, L. R. Performance of Perovskite $CsPbBr_3$ Single Crystal Detector for Gamma-Ray Detection. *IEEE Trans. Nucl. Sci.* **2020**, *67*, 443−449.
(25) Feng, Y.; Pan, L.; Wei, H.; Liu, Y.; Ni, Z.; Zhao, J.; Rudd, P. N.; Cao, L. R.; Huang, J. Low defects density $CsPbBr_3$ single crystals grown by an additive assisted method for gamma-ray detection. *J. Mater. Chem. C* **2020**, *8*, 11360−11368.
(26) Chouhan, L.; Ghimire, S.; Subrahmanyam, C.; Miyasaka, T.; Biju, V. Synthesis, optoelectronic properties and applications of halide perovskites. *Chem. Soc. Rev.* **2020**, *49*, 2869−2885.
(27) Islam, M. J.; Shahjahan, M.; Yuyama, K.; Biju, V. Remote Tuning of Bandgap and Emission of Lead Perovskites by Spatially Controlled Halide Exchange Reactions. *ACS Mater. Lett.* **2020**, *2*, 403−408.
(28) Shahjahan, M. D.; Okamoto, T.; Chouhan, L.; Sachith, B. M.; Pradhan, N.; Misawa, H.; Biju, V. Halide Perovskite Single Crystals and Nanocrystal Films as Electron Donor-Acceptor Heterojunctions. *Angew. Chem.-Int. Edit.* **2022**, *62*, No. e202215947.
(29) Bhagyalakshmi, S. B.; Zhang, D.; Biju, V. Electroluminescence of Halide Perovskite Single Crystals Showing Stochastically Active Multiple Emitting Centers. *J. Phys. Chem. C* **2022**, *126*, 17826−17835.
(30) Shao, Y.; Xiao, Z.; Bi, C.; Yuan, Y.; Huang, J. Origin and elimination of photocurrent hysteresis by fullerene passivation in $CH_3NH_3PbI_3$ planar heterojunction solar cells. *Nat. Commun.* **2014**, *5*, 5784.
(31) Jasik, A.; Sankowska, I.; Pierścińska, D.; Regiński, K.; Pierściński, K.; Kubacka-Traczyk, J. Blueshift of bandgap energy and reduction of non-radiative defect density due to precise control of InAs-on-GaSb interface in type-II InAs/GaSb superlattice. *J. Appl. Phys.* **2011**, *110*, 123103.
(32) Zhang, P.; Zhang, G.; Liu, L.; Ju, D.; Zhang, L.; Cheng, K.; Tao, X. Anisotropic Optoelectronic Properties of Melt-Grown Bulk $CsPbBr_3$ Single Crystal. *J. Phys. Chem. Lett.* **2018**, *9*, 5040.5046.
(33) Peters, J. A.; Liu, Z.; Yu, R.; McCal, K. M.; He, Y.; Kanatzidis, M. G.; Wessels, B. W. Carrier recombination mechanism in $CsPbBr_3$ revealed by time-resolved photoluminescence spectroscopy. *Phys. Rev. B* **2019**, *100*, No. 235305.
(34) Kara, D. A.; Cirak, D.; Gultekin, B. Decreased surface defects and non-radiative recombination via the passivation of the halide perovskite film by 2-thiophenecarboxylic acid in triple-cation perovskite solar cells. *Phys. Chem. Chem. Phys.* **2022**, *24*, 10384−10393.
(35) Yang, L.; Gao, Z.; Zhang, W.; Sun, X.; Wang, Z.; Wang, X.; Xu, B.; Meng, X. Stimulated emission from $CsPbBr_3$ quantum dot nanoglass. *Opt. Mater. Express* **2019**, *9*, 3390−3405.
(36) Lakshmi, D.; Nalini, B.; Jayapandi, S.; Selvin, P. C. Augmented conductivity in $Li_{3x}La_{2/3-x}TiO_3$ nanoparticles: all-solid-state Li-ion battery applications. *J. Mater. Sci.-Mater. Electron.* **2020**, *31*, 1343−1354.
(37) Cheng, P.; Liu, Z.; Kang, R.; Zhou, J.; Zhao, J.; Zuo, Z. Atmospheric All-Solution-Processed Perovskite Light-Emitting Diodes. *Phys. Status Solidi-Rapid Res. Lett.* **2023**, *17*, 2200295.
(38) Xiang, T.; Zhang, Y.; Wu, H.; Li, J.; Yang, L.; Wang, K.; Xia, J.; Deng, Z.; Xiao, J.; Li, W.; Ku, Z.; Huang, F.; Zhong, J.; Peng, Y.; Cheng, Y. Universal defects elimination for high performance thermally evaporated $CsPbBr_3$ perovskite solar cells. *Sol. Energy Mater. Sol. Cells* **2020**, *206*, No. 110317.
(39) Ghosh, S.; Rana, D.; Pradhan, B.; Donfack, P.; Hofkens, J.; Materny, A. Vibrational study of lead bromide perovskite materials with variable cations based on Raman spectroscopy and density functional theory. *J. Raman Spectrosc.* **2021**, *52*, 2338−2347.
(40) Clinckemalie, L.; Valli, D.; Roeffaers, M. B. J.; Hofkens, J.; Pradhan, B.; Debroye, E. Challenges and Opportunities for CsPbBr3 Perovskites in Low- and High-Energy Radiation Detection. *ACS Energy Lett.* **2021**, *6*, 1290−1314.
(41) JAMES, D. W.; SHURVELL, H. F.; PARRY, R. M. Polymorphism in cyclohexanol: A Raman spectroscopic study. *J. Raman Spectrosc.* **1976**, *5*, 201−209.
(42) Gordon, S. H.; Mohamed, A.; Harry-O'Kuru, R. E.; Imam, S. H. A Chemometric Method for Correcting Fourier Transform Infrared Spectra of Biomaterials for Interference from Water in KBr Discs. *Appl. Spectrosc.* **2010**, *64*, 448−457.
(43) Zhang, M.; Zheng, Z.; Fu, Q.; Chen, Z.; He, J.; Zhang, S.; Chen, C.; Luo, W. Synthesis and single crystal growth of perovskite semiconductor $CsPbBr_3$. *J. Cryst. Growth* **2018**, *484*, 37−42.
(44) Estahbanati, M. R. K.; Feilizadeh, M.; Babin, A.; Mei, B.; Mul, G.; Iliut, M. C. Selective photocatalytic oxidation of cyclohexanol to cyclohexanone: A spectroscopic and kinetic study. *Chem. Eng. J.* **2020**, *382*, No. 122732.

https://doi.org/10.1021/acsomega.3c02888
ACS Omega 2023, 8, 26351−26358

(45) Ji, Z.; Cen, G.; Su, C.; Liu, Y.; Zhao, Z.; Zhao, C.; Mai, W. All-Inorganic Perovskite Photodetectors with Ultrabroad Linear Dynamic Range for Weak-Light Imaging Applications. *Adv. Opt. Mater.* **2020**, *8*, 2001436.
(46) Li, G.; Wang, Y.; Huang, L.; Sun, W. Research Progress of High-Sensitivity Perovskite Photodetectors: A Review of Photodetectors: Noise, Structure, and Materials. *ACS Appl. Electron. Mater.* **2022**, *4*, 1485−1505.
(47) Xia, B.; Tu, M.; Pradhan, B.; Ceyssens, F.; Tietze, M. L.; Rubio-Gimenez, V.; Wauteraerts, N.; Gao, Y.; Kraft, M.; Steele, J. A.; Debroye, E.; Hofkens, J.; Ameloot, R. Flexible Metal Halide Perovskite Photodetector Arrays via Photolithography and Dry Lift-Off Patterning. *Adv. Eng. Mater.* **2022**, *24*, 2100930.

https://doi.org/10.1021/acsomega.3c02888
ACS Omega 2023, 8, 26351−26358